A calibrated UV-LED based light source for water purification and characterisation of photocatalysis

A. Sergejevsa, C. T. Clarkea, D. W. E. Allsoppa, J. Maruganb, R. Timmersb, C. Casadob, and C. R. Bowenc

Photocatalysis has a potential to become a cost effective industrial process for water cleaning. One of the most studied photocatalysts is titanium dioxide which, as a wide band gap semiconductor, requires ultraviolet (UV) light for its photoactivation. This is at the wavelengths where the efficiency of present-day light emitting diodes (LEDs) decreases rapidly, which presents a challenge in the use of UV-LEDs for commercially viable photocatalysis. There is also a need for accurate photocatalysis measurement of remediation rates of water-borne contaminants for determining optimum exposure doses in industrial applications. In response to these challenges, this paper describes a UV-LED based photocatalytic test reactor that provides a calibrated adjustable light source and pre-defined test conditions to remove as many sources of uncertainty in photocatalytic analysis and thereby improve data reliability. The test reactor provides a selectable intensity of up to 1.9 kW/m2 at the photocatalyst surface.

1. Introduction

Semiconductor photocatalysts require optical energy to initiate the desired chemical reactions. When excited by light with an energy equal or greater than the band gap of the photocatalyst, electron-hole pairs are produced at the surface. Once generated, the electron-hole pairs initiate reduction and oxidation (redox) reactions [1] that can degrade organic pollutants to intermediate products, even innocuous carbon dioxide. This property of photocatalysts can be advantageous when applied to water purification from organic pollutants [2] ranging from oleaginous contamination [3], pharmaceuticals and personal care products [4,5] through to nonylphenol ethoxylates [6] and inactivation of bacteria such as Escherichia coli [7,8].

One of the most studied photocatalysts is titanium dioxide (TiO_2) due to its attractive properties such as non-toxicity, low cost, stability and suitability for removing organic waste from water [2-5], [7]. However, the absorption characteristics of TiO_2 in its anatase and rutile phases reveal that light with a wavelength shorter than ~365 nm is required for the efficient generation of high densities of electrons and holes [9].

There are several light sources that emit in this wavelength range, but their low efficiency makes them non-optimum for quantifiable photocatalysis. One of the most widely used ultraviolet (UV) light sources is the mercury gas discharge lamp [2-6]. It has multiple spectral components in the UV region of the spectrum as well as visible spectral components [10]. The fact that there are multiple UV spectral components makes mercury gas lamps an unsuitable light source for quantifying photocatalytic experimentation, since it may not be clear which spectral component is responsible for photoactivation. On the other hand, emerging UV light emitting diodes (UV-LEDs) emit near-monochromatic light of an intensity that is determined by the drive current and offers potential advantages for quantifying redox reactions stimulated by photocatalysis [11,12].

A variety of LEDs have been used as a light source for photocatalytic reactions [13]. Obra *et al.* [14] examined a UVA-LED driven photo-Fenton process for micropollutant removal for urban wastewater. High power UVA-LEDs has also been used by Betancourt-Buitrago *et al.* [15] in photoreactors for degradation of methylene blue, who provided a detailed overview of LEDs used in the photodegradation of dyes. The small size of LEDs has attracted interest for photocatalysis since it offers new construction possibilities for characterisation of small volumes of materials [16] at low cost [17,18]. Examples include their use in LED microreactors [19,20], including those based on TiO_2 [21,22] and a low cost device for determination of the quantum yield in photocatalytic and photochemical processes [23]. Organic light emitting diodes (OLEDs) are also being considered [24].

In this paper were report on the design and realization of a multi-LED UV lighting system for enhancing the accuracy and throughput of photocatalytic analysis for dose control. The reactor consists of a light source, a light source controller that stabilizes the temperature and optical power output of the LEDs as well as the uniformity of the illumination reaching the activated surface of the photocatalyst being characterised. The issues of optimum excitation wavelength [12] and the remaining limited efficiency of UV-LEDs and consequent heat generation on system performance are considered in detail.

2. System description

2.1 Design overview

The UV light engine is design for compatibility with a bench-top photocatalytic reactor shown schematically in **Fig. 1a** and **Fig. S1**. The reactor comprises a double wall glass containment vessel for liquid specimens surrounded by an optional opaque shroud to prevent user exposure to potentially damaging intense UV radiation. The hollow wall nature of the containment vessel allows the use of liquid cooling of the sample. The lid of the enclosure holds the UV-LED array at a fixed distance of 7 cm. Despite the recent increase in the efficiency of UV-LEDs [25-27], at best about 70% of their input electrical power is still converted to heat and dissipated in the packaged devices. In addition, at typical operating currents, all III-Nitride based LEDs can suffer further efficiency losses arising from the efficiency droop effect [28]. Any increase in LED temperature due to self-heating or external heating will cause the dominant radiation wavelength to red-shift and thereby reduce near surface absorption of photons in a photocatalyst, such as TiO_2, to decrease its photocatalytic efficiency [2]. Another, potentially more serious problem is the reduction in LED optical power output with increasing junction temperature [29]. These two effects introduce a need for rigorous control of UV-LED heating for accurate photocatalysis measurements. A significant part of the system design, described in more detail in the following sections, addresses the problem of heat extraction from the LEDs and their current drive circuitry.
The light source consists of 36 UV-LEDs mounted on a circuit board in such a way that maximizes both the intensity of the UV illumination and its uniformity over the photocatalyst, which is this work consists of immobilised material (40mm diameter) or a suspension. The following sub-sections detail the optical and electrical design of the UV lighting system.

2.2 System simulation for UV-LED board

Radiation transfer was modeled using the commercial software Ansys Fluent 14.5. The UV-LEDs were simulated as 16 mm diameter surfaces following the specifications of the vendor. Rigorous radiation computations require solution of the radiative transfer equation (RTE) and the discrete ordinates model (DOM) was used to solve the RTE, allowing the evaluation of the radiation field at any point inside the reactor space.

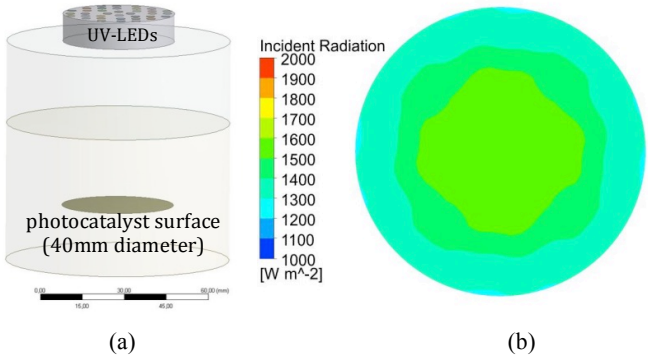

(a) (b)

Fig. 1. (a) computational radiation transfer model (Ansys Fluent) and (b) simulation of the irradiation of the surface of the 40mm diameter photocatalyst, 100mm below UV-LED source. Reactor is also shown in **Fig. S1**.

Results of the simulations shown on **Fig. 1b** revealed that the UV-LED layout illustrated in **Fig. 2** provides a uniform incident irradiation of the surface of the 40 mm diameter photocatalyst. The optimum layout is a compromise between uniformity of illumination and a distribution of UV-LEDs that enables a straight-forward interconnection of the LED groups while also preventing hot spot formation on the circuit board.

The details optimization of the UV-LED layout and reactor geometry by RTE-simulation and experimental measurement will be reported elsewhere.

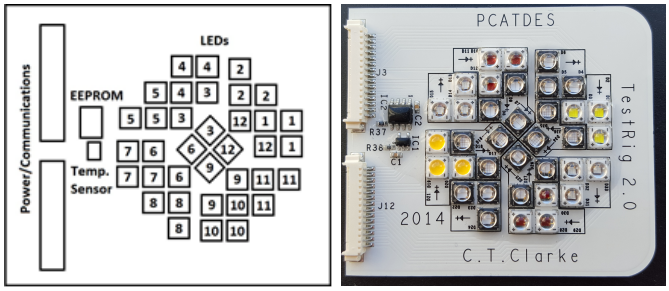

(a) (b)

Fig. 2. (a) schematic of the UV-LED board showing the positions of the LEDs, the EEPROM, temperature sensor and power/communications electronics (see text). The UV-LEDs are numbered in groups showing the channel to which they belong (b) image of UV-LED board.

2.3 UV-LED selection

The coefficient of optical absorption of both the anatase and rutile phases of TiO_2 rapidly increases as the wavelength of UV light reduces from 400 nm to 300 nm. This can be seen in **Fig. 3** (black line) which is data for Degussa P25 which is a commonly used and commercially available photoactive TiO_2 that consists of predominately anatase, along with rutile and a small amount of amporphous phase [30]. This is offset by an even more dramatic decline in the output optical power of many UV-LEDs emitting in the same spectral range. This is also illustrated in Fig. 3 by the emission spectra of three best-of-class commercially available example UV-LEDs with wavelengths of 260 nm (Crystal IS, Inc; blue line) [25], 340 nm (Sensor Electronic Technology, Inc; red line) [26] and 365 nm (LED Engin; green line) [27]. The trend in reduced UV-LED optical power output is mirrored in the state-of-the-art of their fabrication technology [31], [32].

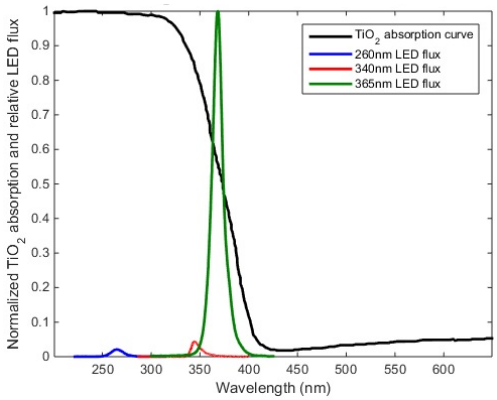

Fig. 3. Wavelength dependence of the optical absorption of Degussa P25 normalized to its nominal value at 250 nm overlaid by the power spectral density of commercially available UV-LEDs emitting at peak wavelengths of 260 nm, 340 nm and 365 nm normalized to the power spectrum of 365 nm wavelength UV-LED [25-27].

The effectiveness of these example UV-LEDs for stimulating photocatalytic reactions can be determined by estimating the near-surface densities of charge carriers generated at each wavelength. We assume only electrons and holes generated in a very thin layer of thickness, w, adjacent to the surface of a TiO_2 particle can trigger redox reactions. The number of electrons (or holes) generated per unit volume, n, from a flux of photons of wavelength, λ, and density, N_o, incident on a semiconductor layer of absorption coefficient $\alpha(\lambda)$ is given by,

$$n(\lambda) = N_o(\lambda)\left(1 - e^{-\alpha(\lambda)w}\right) \qquad (1)$$

Since the wide band gap semiconductors used as photocatalysts are usually not fabricated to the same exacting standards of materials such as silicon or III-V semiconductors, it can be assumed that the carrier lifetime is very short with the effect that only those electrons absorbed in very thin layer

of width close to the surface of the photocatalyst can participate in redox reactions. With the approximation that the product $\alpha(\lambda)w$ is very small (Eqn. 1) can be written as

$$n(\lambda) = N_o(\lambda)\{1 - [1 - \alpha(\lambda)w + \cdots]\} \approx N_o(\lambda)\alpha(\lambda)w \qquad (2)$$

The photon flux density is related to the light intensity, $I_o(\lambda)$, emitted from the UV-LED under consideration via,

$$N_o(\lambda) \sim \frac{\lambda_{peak}}{hc} I_o(\lambda) \qquad (3)$$

The effectiveness of the UV-LEDs for stimulating photocatalytic reactions can therefore be determined by estimating the near-surface densities of charge carriers generated at each wavelength via Eqn. 4, which follows from using Eqn. 3 in Eqn. 2 and integrating the result over the line-width of the LED.

$$n_{surf} = p_{surf} \sim \frac{w\lambda_p}{hc} \int \alpha(\lambda) I(\lambda) d\lambda. \qquad (4)$$

In Eqn. 4, n and p are respectively the densities of photo-generated electrons and holes, λ_p is the wavelength at which the peak intensity of the LED emission occurs, h is Planck's constant, c is the speed of light in free space, $\alpha(\lambda)$ is the wavelength dependent absorption coefficient of the photocatalyst material and the integration is performed over the intensity spectrum, $I(\lambda)$ of the UV-LED under consideration. Table I shows the relative near-surface electron (or hole) densities photocatalytic effectiveness calculated for the three commercially available UV-LEDs with the emission characteristics shown in **Fig. 3**.

Table 1 shown that although more energy per photon is provided to the photocatalyst by the shorter wavelength LEDs, the optical output power of the 260 nm and 340 nm LEDs is too low to compete with the potential photocatalytic performance of recently developed 365 nm wavelength UV-LEDs. For example, devices that can provide up to 1.2 W of optical power for an input electrical power of 2.7 W are now available (LED Engin 365nm LED [16]). Thus, the light output power now available from the chosen UVA LEDs provides significant opportunity to increase the photocatalytic conversion efficiency compared with earlier demonstrations [11,12].

Table 1. Photocatalytic effectiveness of commercially available UV-LEDs (shown in Fig. 3) of different wavelength.

LED emission wavelength (nm)	Optical power output (mW)	Near-surface electron (or hole) density relative to 365nm UV-LED
365	1200	1
340	55	0.049
260	25	0.029

2.4 UV-LED intensity control and driver

To achieve some system simplification, the light source comprises UV-LEDs split into groups (channels) of three LEDs connected in series. Each channel has its own controller (driver) with adjustable drive current to enables control of both the intensity and the distribution of the radiation reaching the photocatalyst surface. Electrical power is delivered to each channel in a quasi-direct current (DC) form that results from filtering a pulse-width modulated (PWM) waveform. This signal is created by a LED driver chip (Texas Instruments LM3405), that is capable of providing 1 A of current at up to 22 V. The PWM duty cycle before filtering controls the average power delivered to the LEDs thus controlling their intensity. The driver includes monitors for voltage and current supplied to LEDs for the fault detection and to enable feedback.

The LED driver chip is driven by a PWM signal from a field-programmable gate array (FPGA) that acts as the main controller for the system. The PWM signal generated by the FPGA acts as a trigger for the LED driver since the FPGA is not capable of providing enough power to the LEDs for their operation at high drive current. The intensity of the LEDs is controlled by adjusting the duty cycle of the PWM signal at a switching frequency of 1 kHz, while the switching frequency of the LM3405 is fixed at 1.6 MHz. The filtered output of the LM3405 ensures that LEDs are driven with a signal with the properties close to that of a direct current.

A switching frequency of 1 kHz was chosen to minimize device heating. Further, it has recently been shown that pulsing the UV light source on-off does not diminish the remediation rate of photocatalysis by TiO_2, indeed it may even enhance it [33].

There is also a temperature monitor on the LED driver boards to protect against circuit overheating. Further protection against overheating is provided by a heat-sink located on the rear side of the driver printed circuit board (PCB). It is a forced convection heat-sink with the air flow is created by the means of two fans in the enclosure of the control electronics.

The FPGA has a "Nios" processor implemented as digital hardware. This processor is responsible for controlling the system and data acquisition from the sensors, as shown in Fig. 4. The Nios processor constantly monitors the state of the sensors on the UV-LED board and UV-LED drivers. If a fault is detected the processor will turn off the UV-LEDs and inform the user about the detected fault. Such feedback is provided through the PC software and through the indicator LEDs on the front panel of the enclosure containing the control electronics. It also controls both the LED and driver cooling. The Nios processor is also responsible for data acquisition from the drift sensor board which is used for calibrating the light source (to be described below). The data is acquired by addressing each individual sensor on the drift board via I2C communications.

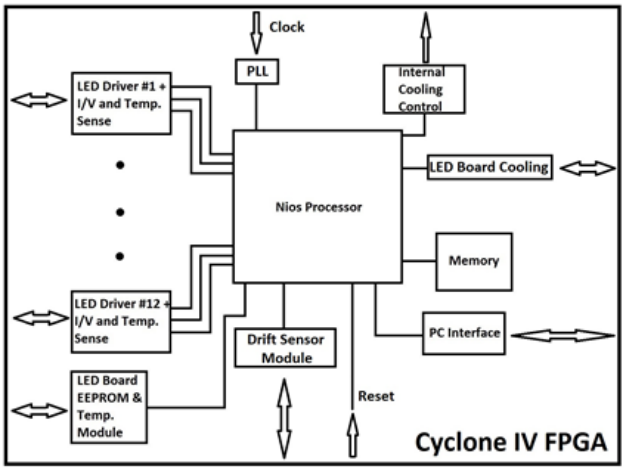

Fig. 4. Block diagram of the FPGA showing the Nios processor, its modules and its sub-system interfaces.

PC software has been created for user interaction with the light source controller and uses a USB protocol to send commands from the PC to the controller and receive data, and allows users to monitor the state of the system as well as set the intensity of each channel independently. The drive current to the strings of LEDs can exceed 0.8 A, at which level the efficiency of the selected UV-LEDs is only ~30%, with the effect that remaining input electrical power is converted to heat dissipated within the LED chips. This has the effect that the optical power density incident on the surface of the photocatalyst will vary with time unless the UV-LED temperature is closely controlled.

2.5 LED circuit board

As mentioned above, there are 36 UV-LEDs on the LED board is controlled via 12 channels comprising three UV-LEDs connected in series. The arrangement of the strings of LEDs is shown in Fig. 2a in which boxes containing the same number represent LEDs in the same channel. When driven at full electrical power each UV-LED outputs 800 mW of optical power in a radiation pattern determined by the lensed encapsulation. This corresponds to 116 mW of UV in the direction of the photocatalyst, which results in ~2.4 W of UV power on the surface of the material. This corresponds to an optical power density of up to ~1.9 kW/m^2 at a wavelength of 365 ± 2 nm at the distance of 0.1 m from the UV-LEDs.

Since the UV-LEDs used in the light source are only 30% efficient, up to ~1.8 W of the input electrical power is wasted as heat from each LED when 1A at 3V are applied. In order to prevent the LEDs from overheating, which results in a red-shift of the dominant radiation wavelength and a reduced optical power output, a separate liquid cooling system (Koolance EX2-755) with a nominal heat extraction rate of 590 W [34] is attached to the back of the LED board. The cooling system is designed to operate with a thermistor as a temperature probe with adjustment of its cooling power based on the voltage drop across the thermistor. It

was found that control of the LED cooling system with a digital potentiometer (Analog Devices AD7376ARUZ10) reliably mimics the circuit performance of a thermistor.

The LED board is an Insulated Metal Substrate (IMS) printed circuit board (PCB) for improved thermal management. Since the performance of the LEDs is heat sensitive [29], a temperature sensor is placed on the PCB on which the UV-LEDs are mounted. The sensor is used for overheating protection, whereby if the temperature of the PCB reaches a pre-defined value (60°C), the electrical power to the LEDs will be switched off until the PCB cools down and user actively turns it on again. Since the temperature sensor is located at a distance from the UV-LEDs it can only measure the temperature of PCB board, rather than the usually much higher junction temperatures the LEDs. A cut-off value of 60°C was chosen by determining the PCB temperature at the intensity of the light output of the 36 UV-LED system was unchanged as the drive current to all 12 LED channels was increased.

Measurements of the LED optical power versus current characteristics revealed that there is a ±10% variation in their optical power output at the same drive current, as well as ±2 nm variation in the dominant emission wavelength in even a small batch of devices; see **Fig. S2** for example. In order to achieve a better control of the optical power delivered to the photocatalyst, an electrically erasable programmable read-only memory (EEPROM) chip is added to the LED light source circuit. The EEPROM holds calibration information that is used to estimate the intensity of each channel at different electrical power levels and the offset of the emission wavelength from the nominal value (365 nm); see **Fig. S3** for a memory map of the EEPROM. Using this information and the fact that each LED channel has its own driver, the controller is able to adjust the input power to any channel and thus minimize the non-uniformity across the surface of the photocatalyst. Placement of the EEPROM chip on the LED board (see **Fig. 2a**) ensures that the calibration information stays with the light source. This allows the UV light source to be used with a different controller yet maintain the same performance.

2.6 Drift sensor

During extended use the intensity and wavelength of a UV-LED can degrade [35] and such changes will affect the outcome of measurements of photocatalytic behavior. In order to ensure that the UV-LED characteristics have not changed significantly, a drift sensor was incorporated into the system. This sensor consists of 12 ambient light sensors (Avago Technologies APDS-9301-020) comprising two photodiodes, one sensitive to visible light, the other sensitive to UVA light with the latter used for calibrating the UV light source [35]. The sensor communicates with the control electronics via Inter-Integrated Circuit (I2C) communications protocol.

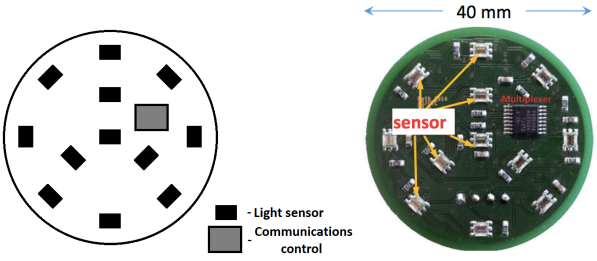

(a) (b)

Fig. 5. (a) schematic of sensor board with light sensors (indicated) distributed evenly across the board (b) image of drift sensor.

The drift sensor is made in the form of a disk as shown in **Fig. 5** in order to fit into the photocatalyst sample holder. Although the drift sensor provides only a relative measurement of the UV-LED intensity, since the responsivity of the UVA photodiode has not been calibrated against a light source with a known power output, this is sufficient to ensure that the variation in intensity of UV light produced by different LED boards is within ±2% of a user-defined value. Its other uses are to enable additional checks of relative UV-LED intensity, the uniformity of light distribution across the photocatalyst and acquiring of calibration data that is stored in the EEPROM. The drift sensor can also be used for recalibration of the system.

3. System performance

3.1 Calibration of system

Several factors need to be taken into account when using the drift sensor to calibrate the 36 UV-LED light source. First, LED-to-LED variations in optical power output need to be balanced out and, second, geometric factors need to be account for. The latter include skewing of the ±45° emission cone (**Fig. 6a**) of individual UV-LEDs from the surface normal of the LED circuit board. The skewing arises from non-optimum soldering the UV-LEDs onto the circuit board and from misalignment of the lenses used in the device packages to maximize the optical power radiated into a ±45° cone about the nominal UV-LED surface normal. These factors combine to cause significant non-uniformity in the intensity distribution over the surface of the photocatalyst

In addition, the use of a drift sensor to calibrate the lighting system requires the dependence of the photocurrent generated in a given photodiode on the relative positions of its 12 photodetectors and the three UV-LEDs in a selected channel (**Fig 6b**).

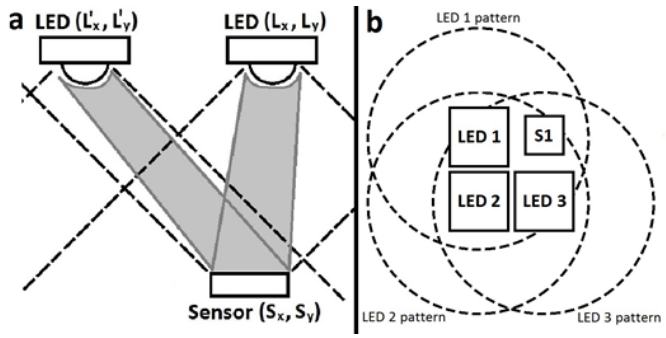

Fig. 6. (a) schematic of the relative positions two LEDs with respect to an individual sensor, (b) use of a drift sensor (S1) to calibrate the lighting system from the dependence of the photocurrent in a given photodiode on the relative positions of its 12 photodetectors and three UV-LEDs in a selected channel.

Fig. 7a shows an example of the intensity distribution across the 40 mm diameter surface measured by the drift sensor for one LED channel (LEDs labelled "1" in **Fig. 7b** which replicates **Fig. 2a** to enable immediate visual comparison) excited by a 50 mA drive current. **Fig. 7c** shows the intensity map for the channel located diametrically opposite on the circuit board (LEDs labelled "7" in **Fig. 7b**) when excited by the same 50 mA drive current. Due to the symmetry of the layout of the LEDs on the circuit board, this should be an inverse intensity map. However, **Fig. 7d** shows that whilst the combined optical power distributions of the two oppositely located channels produces an intensity peak at the center of the photocatalyst holder, the equal intensity contours are skewed towards lower left.

The calibration procedure, now described, compensates for (a) the detector-LED alignment problem, (b) the variations in the electrical-to-optical power conversion efficiency of each channel and (c) any skewing of the radiation from particular channels. First, the optical power received by each of the 12 photodiodes on the drift sensor board is measured as each channel is excited in turn with a range of input currents up to 500 mA. The resulting optical power output versus drive current characteristic of every channel is then stored in the EEPROM on the LED circuit board.

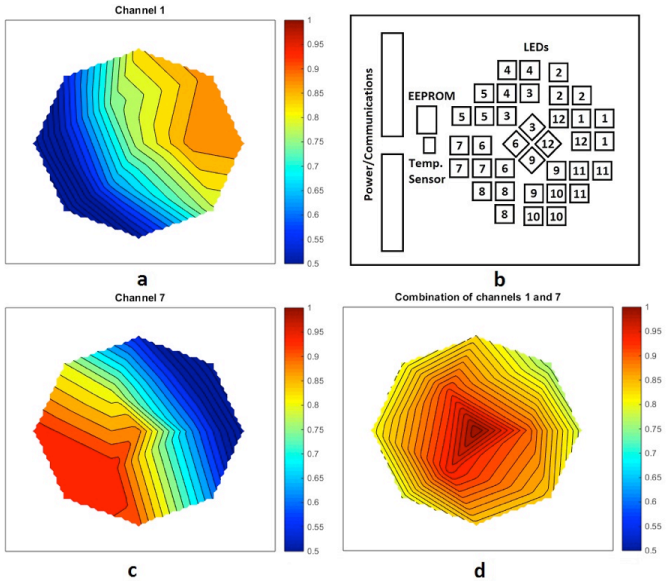

Fig. 7. Normalized light distribution over the area of the drift sensor located in the photocatalyst holder from (a) Channel 1, (c) Channel 7, which are located opposite each other on the LED board (b) at the same intensity level. Resulting illumination of the drift sensor from both Channel 1 and 7 simultaneously in (d).

Next, the contribution of the three UV-LEDs in a channel to the optical power, at a fixed drive current, incident on each of the 12 sensors on the drift sensor is calculated from the radiation pattern of LEDs from the manufacturer's datasheet [26] and the photodiode responsivity, also taken from its manufacturer's datasheet [36]. This was repeated for every LED channel to find the theoretical contribution of each UV-LED to the total optical power incident on each of the 12 photodiodes on the drift sensor board shown in **Fig. 5**. From these, data correction factors were calculated to apply to the drive current to the LED channels and thereby equalize the optical power received by the 12 photodiodes of the drift sensors.

It was found that the correction factors were dependent on the drive currents applied to the channels, owing to variation in the light output-current-voltage characteristics of the LEDs. Therefore, the procedure was repeated for a range of drive currents up to the 500 mA maximum to enable users to select the optical power level at the surface of the photocatalyst. Quadratic lines of best fit to the drive current dependence of the corrections factors of each channel were then constructed and the curve fitting coefficients stored in the EEPROM to enable selection of a desired optical power output via the user interface.

Fig. 8a shows the variation in the measured output intensities of the 12 channels on the LED circuit board with the user-defined (i.e. user-set) power level before the calibration is applied. The error bars on the data points do not represent the random errors in the measurement optical output power, which is in fact measured to better than 1% accuracy. Instead the "error bars" show the typical comparative range of the un-calibrated output power of each channel, i.e. each group of three LEDs, operating at nominally the same user-set intensity. In **Fig. 8a**, each 1% set intensity corresponds to a drive current increment of 10 mA. In other words, the observed range is actual rather than user-set intensity and demonstrates the need for rigorous light-source calibration procedure for fully quantitative measurements of photocatalytic reactions. The straight line corresponds to the unity gradient trend line between user-set and measured optical output power that would be obtained if each channel was perfectly calibrated.

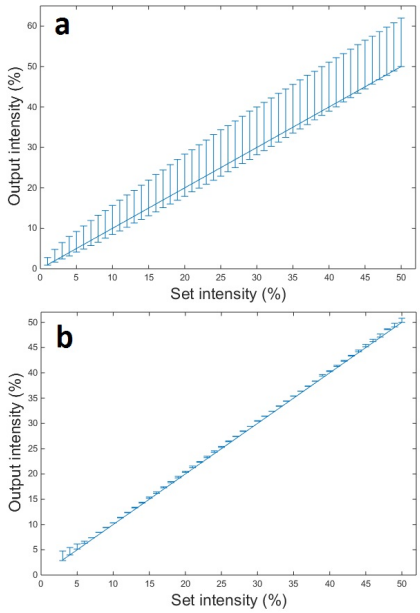

Fig. 8. Comparison of UV-LED intensity output errors of the 12 channels on the LED circuit board before (a) and after (b) calibration.

Fig. 8b shows the impact of applying the calibration procedure. The measured output intensity at each of the user-set power levels now closely match the one-to-one trend line of a perfectly calibrated system. The only performance cost of calibration procedure is the reduction in total achievable output power which comes from matching the optical power output of every channel to that of the worst performing one. Overall, the measured intensity values are within ±0.5% of the set value over a drive current range of up to 500 mA.

3.2 Application to remediation of simulated palm oil mill effluent

The reactor design and UV calibration makes it possible to use on both immobilised materials and conventional suspensions. As a demonstration, the bench-top photocatalytic reactor with its calibrated 36 UV-LED light source has been applied to quantifying the degradation of cinnamic acid using 0.1 $g \cdot L^{-1}$ of Degussa P25 commercial TiO_2. Cinnamic acid was chosen as model of phenolic compounds usually present in wastewater from palm oil industry at concentrations in the range of 50—200 mg/L, although it depends of the type of extraction process used. These compounds, present in effluents and landfills, are difficult to degrade and toxic to most microorganism present in water, and are of increasing environmental concern [37, 38].

Fig. 9 shows that a 90% of reduction of cinnamic acid concentration can be achieved within 30s at room temperature when the 36 UV-LED source is working at maximum calibrated emission power (100%). The combination of the stability of the UV light source, particularly its temperature control, and the temperature control of the reaction mixture achieved via the dual-wall design of the reactor provided the stability that allows the use of high irradiation power, to bring about an increase of photo-activity. Such UV-LED based bench-top reactors will contribute to better quantification of photocatalytic reactions to enable correct design of industrial processes for adequately cleaning the water-based effluent from various industrial processes to meet the environmental standards of cleanliness prior to being released rivers and aquifers. Indeed, a flow-through photocatalytic reactor that can work either with a supported catalyst, or as a slurry photo-reactor with a high intensity UV-LED illumination of the entire reactor volume has now been realized with its design based on the calibrated bench-top reactor described here.

4. Conclusions

This work describes a UV-LED based photocatalytic test reactor that provides a calibrated adjustable UV light source and pre-defined test conditions to remove as many sources of uncertainty in photocatalytic

analysis and thereby improve data reliability. It is shown that UV-LEDs emitting at a nominal wavelength of 365 nm have the potential to provide a rugged and high efficiency light source suitable for quantifying and calibrating photocatalytic purification of water-borne effluent. The demonstrated UV-LED system design includes a sensor board that enables the calibration of a 36-LED light source to correct for the variation in the individual UV-LED characteristics used arising from manufacturing process variability and skewing of the light emission from its ideal alignment to the surface normal of the circuit board on which the LEDs are mounts. The resulting calibration results in the illumination a 40 mm diameter photocatalyst placed 100 mm the LED circuit board with UV light of intensity in the range 0.048 – 2.4 W with a uniformity over the catalyst of ±2%. Further, the measured output intensity replicates user-defined optical power levels to an accuracy of ±0.5%. The test reactor therefore provides a selectable intensity of up to 1.9 kW/m^2 at the material surface for reliable and robust photocatalyst analysis.

Acknowledgements

This work was supported by The European Union under FP7 Project 309846, "Photocatalytic materials for the destruction of recalcitrant organic industrial waste (PCATDES)".

References

1 M. M. Haque, D. Bahnemann, M. Muneer, Photocatalytic degradation of organic pollutants: Mechanisms and kinetics, in organic pollutants ten years after the Stockholm Convention – Environmental and analytical update, Rijeka, Croatia: InTech, 2012, ch. 12, sec. 3, pp. 293-326.
2 Y. Meng, Y. Wang, Q. Han, N. Xue Y. Sun, et. al, Trihalomethane (THM) formation from synergic disinfection of biologically treated municipal wastewater: Effect of ultraviolet (UV) irradiation and titanium dioxide photocatalysis on dissolve organic matter fractions, *Chem. Eng. Journal*, 2016, , 252-260.
3 M. N. Chong, B. Jin, C. W. K. Chow, C. Saint, Recent developments in photocatalytic water treatment technology: A review, *Water Research*, 2010, **44**, 2997-3027.
4 N. Miranda-García, S. Suárez, M. Ignacio Maldonado, S. Malato, B. Sánchez, Regeneration approaches for TiO_2 immobilized photocatalyst used in the elimination of emerging contaminants in water, *Catal. Today*, 2016, **303**, 252–260.
5 R. Bautista, W. Anderson, S. Pagsuyoin, and J. Munoz, Degradation of tetracycline in synthesized wastewater using immobilized TiO_2 on rotating corrugated aluminum drum", IEEE Systems and Information Engineering Design Symposium, 2015.
6 A. Ashar, M. Iqbal, I. A. Bhatti M. Z. Ahmad, K. Qureshi, J. Nisar, I. H. Bukhari, Synthesis, characterization and photocatalytic activity of ZnO flower and pseudo-sphere: Nonylphenol ethoxylate degradation under UV and solar irradiation, *J. Alloys Compds.*, 2016, **678**, 126-136.
7 R. van Grieken, J. Marugán, C. Sordo, C. Pablos, Comparison of the photocatalytic disinfection of E. coli suspensions in slurry, wall and fixed-bed reactors, *Catal. Today*, 2009, **144**, 48-54 .
8 C. Adán, J. Marugán, S. Obregón, G. Colón, Photocatalytic Escherichia coli inactivation by means of trivalent Er^{3+}, Y^{3+} doping of $BiVO_4$ system, *Appl. Catal. A: General*, 2016, **526**, 126–131.
9 B. Choudhury and A. Choudhury, Tailoring luminescence properties of TiO_2 nanoparticles by Mn doping, *J. Lumin*., 2013, **136**, 339-346.
10 C. J. Sansonetti, M. L. Salit, J. Reader, Wavelengths of spectral lines in mercury pencil lamps, *Appl. Opt*., 1996, **35**, 74-77.
11 K. Dai, L. Lu, G. Dawson, Development of UV-LED-TiO_2 device and their application for photocatalytic degradation of methylene blue, *J. Mat. Eng. and Perf*., 2013, **22**, 1035-1040.
12 M. R. Eskandarian, H. Choi, M. Fazli, M. H. Rasoulifard, Effect of UV-LED wavelengths on direct photolytic and TiO_2 photocatalytic degradation of emerging contaminants in water, *Chem. Eng. Journal*, 2016, **300**, 414-422.
13 S. Landgraf, Application of semiconductor light sources for investigations of photochemical reactions, *Spectrochimica Acta Part A,* 2001, **57**, 2029–2048.
14 I. de la Obr, B. Esteban García, J. L. García Sánchez, J. L. Casas López, J. A. Sánchez Péreza, Low cost UVA-LED as a radiation source for the photo-Fenton process: a new approach for micropollutant removal from urban wastewater, *Photochem. Photobiol. Sci*., 2017, **16**, 72-78.
15 L. A. Betancourt-Buitrago, C. Vásquez, L. Veitia, O. Ossa-Echeverry, J. Rodriguez-Vallejo, J. Barraza-Burgos, N. Marriaga-Cabrales, F. Machuca-Martínez, An approach to utilize the artificial high power LED UV-A radiation in photoreactors for the degradation of methylene blue, *Photochem. Photobiol. Sci*., 2017, **16**, 79-85.
16 O. Shvydkiv, A. Yavorskyy, K. Nolan, A. Youssef, E. Riguet, N. Hoffmann, M. Oelgemo¨ller, Photosensitized addition of isopropanol to furanones in a 365 nm UV-LED microchip, *Photochem. Photobiol. Sci*., 2010, **9**, 1601–1603.
17 M. Gombár, É. Józsa, M. Braun, K. Ősz, Construction of a photochemical reactor combining a CCD spectrophotometer and a LED radiation source, *Photochem. Photobiol. Sci*., 2012, **11**, 1592-1595.

18 J. M. Carney, R. J. Hammer, M. Hulce, C. M. Lomas, D. Miyashiro, High-efficiency microphotooxidation using milliwatt LED sources, Tetrahedron Letters, 2011, **52**, 352–355.
19 Y. Matsushita, N. Ohba, S. Kumada, K. Sakeda, T. Suzuki, T. Ichimura, Photocatalytic reactions in microreactors, *Chem. Eng. Journal*, 2008, **135S**, S303–S308.
20 J. M. Carney, R. J. Hammer, M. Hulce, C. M. Lomas, D. Miyashiro, Microphotochemistry using 5-mm light-emitting diodes: Energy-efficient photooxidations, *Synthesis*, 2012, **44**, 2560–2566
21 M. Krivec, K. Žagar, L. Suhadolnik, Mi. Čeh, G. Drazĭc, Highly efficient TiO_2-based microreactor for photocatalytic applications, *ACS Appl. Mater. Interfaces* 2013, **5**, 9088–9094.
22 H. Eskandarloo, A. Badiei, M. A. Behnajady, G. M. Ziarani, UV-LEDs assisted preparation of silver deposited TiO_2 catalyst bed inside microchannels as a high efficiency microphotoreactor for cleaning polluted water, *Chem. Eng. Journal*, 2015, **270**, 158–167.
23 U. Megerle, R. Lechner, B. Ko¨nig, E. Riedle, Laboratory apparatus for the accurate, facile and rapid determination of visible light photoreaction quantum yields, *Photochem. Photobiol. Sci*., 2010, **9**, 1400–1406.
24 D. Ziegenbalg, G. Kreisel, D. Weiß, D.Kralisch, OLEDs as prospective light sources for microstructured photoreactors, *Photochem. Photobiol. Sci*., 2014, 13, 1005-1015.
25 Datasheet Klaran UVC Light Emitting Diodes, Crystal IS Inc., NY, U.S.A., (2016: Dec) [Online]. Available from: http://www.cisuvc.com/content/documents/files/CIS.KlaranLEDS.DS.8.3.pdf [March 2017]
26 Datasheet UVA 340 nm LEDs, Sensor Electronic Technology, Inc, GA, U.S.A., (2016: Dec) [Online]. Available from: http://www.s-et.com/products/datasheets/340nm/UVPKG_CUD4AF1B_R00.pdf [March 2017]
27 Datasheet LZ1-00UV00 LED, LED Engin Inc., CA, U.S.A., [Online]. Available from: http://www.ledengin.com/files/products/LZ1/LZ1-00UV00.pdf [March 2017]
28 G. Verzellesi, D. Saguatti, M. Mengeghini, F. Bertazza, M. Goano, G. Meneghesso E. Zanoni, Efficiency droop in InGaN/GaN blue light-emitting diodes: physical mechanisms and remedies, *J. Appl. Phys.*, 2013, **114**, 071101.
29 Thermal characteristics of LEDs (presentation), OSRAM Opto Semiconductors GmbH., Regensberg, Germany. [Online]. Available from: http://ledlight.osram-os.com/wp-content/uploads/2013/01/OSRAM-OS_LED-FUNDAMENTALS_Thermal-Characteristics-of-LEDs_v2_08-16-11_SCRIPT.pdf [March 2017]
30 B. Ohtani, O. O. Prieto-Mahaney, D. Li, R Abe, What is Degussa (Evonik) P25? Crystalline composition analysis, reconstruction from isolated pure particles and photocatalytic activity test, *J. Photochem. and Photobiol. A*: Chemistry, 2010, **216**, 179-182.
31 H. Hirayama, N. Maeda, S. Fujikawa, S. Toyoda, N. Kamata, Recent progress and future prospects of AlGaN-based high-efficiency deep-ultraviolet light-emitting diodes, *Japan. J. Appl. Phys.*, 2014, **53**, 100209.
32 M. Kneissl, A brief review of III-nitride UV emitter technologies and their applications, in III-Nitride Ultraviolet Emitters: Technology and Applications, M. Kneissl and J. Rass Eds., Berlin, Springer-Verlag, 2016, DOI: 10.1007/978-3-319-24100-5, pp 1-25.
33 Y. Ku, S.-J. Shiu, H.-C. Wu, Decomposition of dimethyl phthalate in aqueous solution by UV-LED/TiO_2 process under periodic illumination, *J. Photochem. and Photobiol. A: Chemistry*, 2017, **332**, 299-305.
34 Koolance EX2-755 Specifications [Online]. Available from: http://koolance.com/ex2-755-exos-2-v2-liquid-cooling-system-aluminum [March 2017]
35 D. Renoux, Report on methods for accelerated ageing tests of SSL, A report of the EMRP Joint Research Project, Metrology for Solid State Lightning, 2013, [Online]. Available from:http://www.m4ssl.npl.co.uk/wpcontent/uploads/2013/04/ENG05_D246_v11.pdf [March 2017]
36 Datasheet APDS-9301 Miniature ambient light photo sensor with digital (I2C) output, Broadcom Limited, CA, U.S.A., (2016, Dec) [Online]. Available from: http://www.farnell.com/datasheets/1816958.pdf?_ga=1.110989318.2092180984.1481112455 [March 2017]
37 E. Ugazio, M.E. Carlotti, S. Sapino, M. Trotta, D. Vione, C. Minero, Photodegradation of cinnamic acid in different media, *J. Dispersion Sci. Technol*, 2008, **29**, 641-652.
38 F. Cermola, M. Dellagreca, M.R. Iesce, S. Montella, S. Pollio, F.A. Temussi, A mild photochemical approach to the degradation of phenols from olive oil mill wastewater, *Chemosphere*, 2004, **55**, 1035-1041.